



PCCP

First-principles based Monte Carlo modeling of the magnetization of oxygen-deficient Fe-substituted SrTiO₃

Journal:	<i>Physical Chemistry Chemical Physics</i>
Manuscript ID	CP-ART-03-2023-001078.R1
Article Type:	Paper
Date Submitted by the Author:	03-Jul-2023
Complete List of Authors:	Florez, Juan; Universidad Tecnica Federico Santa Maria, Physics Solis, Miguel; Universidad Tecnica Federico Santa Maria, Physics Cortés, Emilio; Universidad Tecnica Federico Santa Maria, Physics Suarez Morell, Eric; Universidad Tecnica Federico Santa Maria, Fisica Ross, Caroline; MIT,

SCHOLARONE™
Manuscripts

Cite this: DOI: 00.0000/xxxxxxxxxx

First-principles based Monte Carlo modeling of the magnetization of oxygen-deficient Fe-substituted SrTiO₃

Juan M. Florez ^{a,*}, Miguel A. Solis ^a, Emilio A. Cortés Estay ^a, E. Suárez Morell ^{a,b} and Caroline A. Ross ^c

Received Date

Accepted Date

DOI: 00.0000/xxxxxxxxxx

Transition-metal (TM) substituted SrTiO₃ has attracted much attention because its magnetism and/or ferroelectricity can be tuned via cation substitution, point defects, strain and/or oxygen deficiency. For example, Goto et al. [Phys. Rev. Applied 7, 024006 (2017)] reported the magnetization of SrTi_{1-x}Fe_xO_{3-δ} (STF) grown under different oxygen pressures and on various substrates. Here, we use hybrid density functional theory to calculate the effects of different oxygen vacancy (v_o) states in STF on the magnetization for a variety of Fe cation arrangements. The magnetic states of the cations associated with the v_o ground-states for $x = \{0.125, 0.25\}$ are used within a Monte Carlo model for collinear magnetism to simulate the spontaneous magnetization. Our model captures several experimental features of STF, i.e., an increase in magnetization for small δ up to a maximum of $\sim 0.35\mu_B$ per formula unit at an intermediate number of vacancies, with a slower decrease in magnetization with increasing number of vacancies. Our approach gives insight into the relation between vacancy concentration and the oxygen pressure required to maximize the magnetization.

1 Introduction

Perovskite-structured oxides exhibit an exceptionally rich variety of electronic properties including ferroelectricity¹⁻⁴, magnetic order⁵⁻⁸, superconductivity⁹⁻¹², and multiferroicity^{5,13,14}, properties that can be tuned via the composition, doping, strain state, and defect population of the material^{13,15-21}. One of the cornerstone materials of oxide electronics is SrTiO₃ (STO) which has a large bandgap and nonmagnetic behavior at room temperature²². STO can be integrated with Si devices, and ferroelectric and magnetic behavior can be promoted by strain and by magnetic substitution, respectively^{5,13,21-23}. Recent work has focused on the role of oxygen-defects and substitution for Ti on the multiferroic properties^{13,16-21,23-31}, and an interplay between the oxygen stoichiometry and the magnetic and ferroelectric degrees of freedom has been demonstrated.

A stoichiometric oxygen content in ABO₃ perovskites was thought to be a key to obtain robust magnetic order³², and the introduction of oxygen vacancies (v_o) or cation defects usually led to weak magnetic ordering or paramagnetic-like states^{13,33}.

However, experimental results have shown that O-deficiency is capable of turning a magnetic semimetal such as SrCoO₃ (SCO) into a semiconductor as well as converting the insulating paramagnetic STO into a magnetic semiconductor or weak ferroelectric^{5,23,34}. 3d-orbitals in transition metal (TM) cations are distorted by incomplete oxygen octahedral coordination O_{5,4}, and both the covalent and ionic bonding characteristics of O-A/B- v_o defects play a role³⁵, as in the case of SCO³⁴ and Fe,Co-substituted STO^{6,36}.

Defects in ABO₃ perovskites affect other ferroic orders. At low temperatures, stoichiometric STO presents antiferrodistortive structural changes and quantum fluctuations that suppress the ferroelectric (FE) ordering^{37,38}, and coupling of interstitial and anti-site Ti with Sr and O vacancies has been suggested to promote polar effects beside magnetism³⁹⁻⁴⁴. Multiferroic oxygen deficient SrFeO₃ nanoparticles⁴⁵ displayed a saturation electric polarization that depended on the Fe concentration³⁰. Electric polarization was realized in magnetic Fe-doped Ti-rich STO at room temperature⁴⁶. Among TM-substituted STO, SrTi_{1-x}Fe_xO_{3-δ} (STF) and SrTi_{1-x}Co_xO_{3-δ} (STC) both display magnetization that depends on their oxygen content^{13,34,47}.

In this work, we focus on modeling the magnetic properties of STF. Its magnetic properties can be varied via both cation composition and O deficiency. Room temperature magnetism and anisotropy with out-of-plane magnetic easy axis are observed

^a Grupo de Simulaciones, Departamento de Física, Universidad Técnica Federico Santa María, Valparaíso 2390123, Chile

^b Departamento de Física Aplicada I, Escuela Politécnica Superior, Universidad de Sevilla, España

^c Department of Materials Science and Engineering, Massachusetts Institute of Technology, 77 Massachusetts Avenue, Cambridge, Massachusetts 02139, USA

* Corresponding author: juanmanuel.florez@usm.cl

in thin films of nondilute STF and STC deposited on different substrates. The magnetization of STC and STF increases with the Co or Fe content, and is higher for lower growth pressure and therefore greater oxygen vacancy concentration, although for STF a decrease in magnetization was found at the lowest growth pressures^{13,33,34,48–50}. Using X-ray magnetic circular dichroism (XMCD) we showed that the magnetic moment in STF was proportional to the concentration of divalent Fe which increased in films grown at low pressures or annealed in a reducing environment^{13,33}. The magnetic properties are intrinsically tied to the mixture of valence and spin states and their corresponding ferromagnetic (FM) or antiferromagnetic (AFM) local spin-ordering, which strongly depends upon the oxygen vacancies coordinating the transition metal ions. A comprehensive model of the effects of vacancy distribution on the ferroic order parameters remains a challenge.

We theoretically investigate the saturation magnetization of STF. First, we use hybrid-DFT methods to obtain the STF spin-states, local magnetic ordering, and energetically favored TM symmetry and defect formation; then we use that microscopic information to feed an intuitive statistical model for the magnetization, whose probability distribution is calculated by using a Monte Carlo method that samples over the vacancy configuration space for any given number of vacancies, while fulfilling the limitations of symmetry and magnetic configurations imposed by the ground state solutions. The nonmonotonic dependence of the STF magnetization on oxygen pressure has not been adequately addressed, due to the large configurational space to be considered and the complex relation between deposition process parameters and point defect populations. Our microscopic and statistical approaches give a good agreement with STF experiments and might apply to other ABO₃ systems.

This article is organized as follows: In section 2 we introduce the perovskite model, the DFT methods, and the MC approach. In section 3 we show the DFT results for stoichiometric and oxygen-deficient systems with $\delta = \{0, 0.125\}$, and $x = \{0.125, 0.25\}$. In section 4 we present the MC statistical analysis for the STF magnetization. In section 5 the conclusions are presented.

2 Modeling framework

We use density functional theory with a Heyd-Scuseria-Ernzerhof (HSE06) exchange-correlation functional as implemented in the Vienna Ab-initio Simulation Package (VASP 5.4)^{52–54} to study the effects of oxygen deficiency in STF. The use of a hybrid functional leads to improved accuracy over standard local and semi-local functionals such as LSDA, GGA or Perdew-Burke-Ernzerhof (PBE) for predictions of key properties such as valence spin-states, chemical-induced structural changes and band-gaps in 3d-oxides as shown previously e.g., for SCO, STO, STC and SrTi_{1-x-y}Fe_xCo_yO_{3- δ} (STFC)^{13,34,36}. We also performed GGA+U calculations in order to examine the stability of selected Fe spin-states under strain for the sake of discussion, because use of the HSE06 functional incurs large computational costs compared to local methods.

The spin-polarized calculations were performed with an energy cutoff of 500 eV for $2 \times 2 \times 2$ and $4 \times 4 \times 4$ k-point grids in the case of HSE06, for relaxations and static calculations, respectively, and $6 \times 6 \times 6$ for GGA+U in both cases. The HSE06 grids were chosen to keep the computational costs at a reasonable level, and the results represent converged relaxations with forces below 10^{-4} eV/Å. A screening value μ of 0.207 (Å⁻¹) with a 25% Hartree-Fock exact exchange were selected such that those reproduce the calculations in the References^{13,34} for ST(F,C)/STO, and the $U_{eff} = U - J$ terms were used within Dudarev's GGA+U approach for the Fe *d* electrons⁵⁵. In the latter case, the acting forces were reduced below 10^{-5} eV/Å, and the U_{eff} values were chosen within the range of validity of recent simulations for other Fe-substituted STO compounds i.e., 4 and 7 eV for 3*d*-orbitals were applied to Fe and Ti, respectively^{6,56}. In the case of the ab-initio calculations, the supercell of the solid solutions consisted of $2 \times 2 \times 2$ unit cells with {40,39} ions for $\delta = \{0.0, 0.125\}$, as displayed in Figure 1. PBE pseudopotentials were used with $3s^2 4p^6 5s^2$, $3d^3 4s^1$, $3d^7 4s^1$, and $2s^2 2p^4$ distributions for Sr, Ti, Fe, and O respectively.

The positions of the oxygen vacancies, shown in lower panels of Figure 1 as $V_{a,p,d(1,2)}$, were selected after a symmetry analysis of the relaxed stoichiometric (i.e. no vacancies) systems corresponding to three different distributions of the Fe cations within the supercells for %25 Fe substitution, obtained with FINDSYM and pymatgen applications^{57–59} for a 10^{-3} Å tolerance. The Fe-nearest-neighbor (nn) distances considered were $\{a, \sqrt{2}a, \sqrt{3}a\}$, with *a* the initial unit-cell parameter. According to each configuration, we have considered all the atomic valence states, which are reflected in several possible high and low Pauli states for the TM, as well as the possible combinations for the FM or AFM Fe-Fe exchange coupling. The valences of the cations are selected to maintain a neutral supercell for a given oxygen deficiency, and point/bulk-charging effects due to these defects are negligible as suggested by DFT calculations in STF and STFC^{6,36}. We also refer in this work, without loss of generality, to $V_{a,p,d(1,2)}$ as the vacancies corresponding to the Fe cations aligned along the [1,0,0] (above), [1,1,0] (plane) and [1,1,1] (diagonal) crystalline directions, respectively.

To model the magnetic order parameter we use Monte Carlo (MC)⁶⁰ calculations to extract ν_O -configurational probabilities for specific cation distributions and using $4 \times 4 \times 4$ supercells as displayed in the upper panels of Figure 1. Within a Metropolis⁶¹ scheme an algorithm with an aleatory-sampling acceptance $\text{rand}(0,1) \leq \exp(-\Delta E/k_B T)$ is implemented. Here the ΔE energies are obtained from ab-initio characterization, such that they discriminate the states corresponding to FM from the AFM ones, as well as the lowest-energy states (gs) from second to lowest solutions (ss), for a representative group of ν_O out of all the $V_{a,p,d(1,2)}$ possibilities.

Our MC simulation works by extracting oxygen ions from the lattice similar to how a Galton-board arranges balls⁶², where the

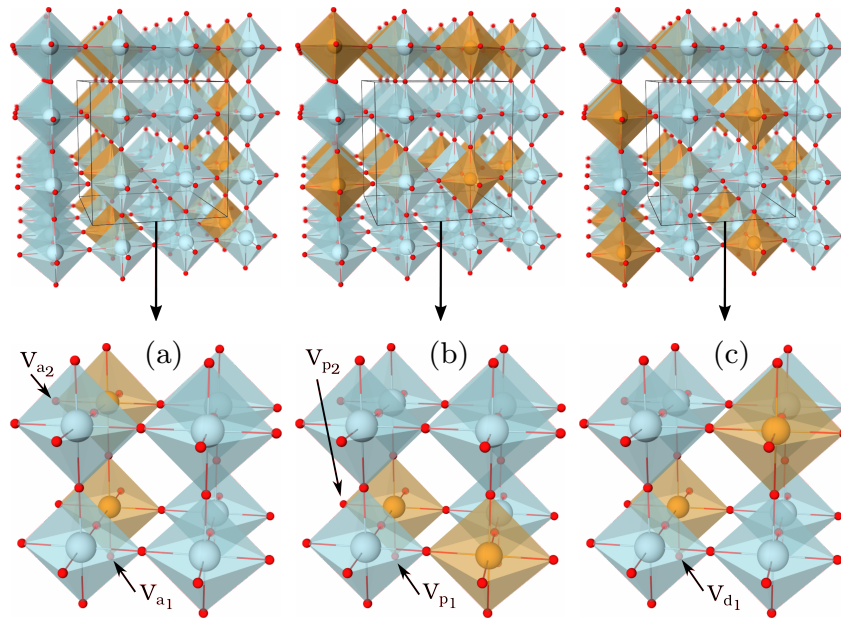


Fig. 1 Supercell for $x = 0.25$ in $\text{SrTi}_{1-x}\text{Fe}_x\text{O}_{3-\delta}$: (a) Fe-Fe pair with $m_{\text{Fe}} = a$. (b) Fe-Fe pair with $m_{\text{Fe}} = a\sqrt{2}$; and (c) Fe-Fe pair with $m_{\text{Fe}} = a\sqrt{3}$. a is initially the STO lattice parameter. The vacancies are depicted as: $V_{a1,2}$, $V_{p1,2}$ and V_{d1} , respectively. The Sr atoms have been omitted for the sake of simplicity. Graphical representations were produced using the OVITO software⁵¹.

resulting ball-filled columns' heights would represent the different v_{O} -configurational probabilities for a certain number of vacancies arranged in the octahedra. As such, for a given adiabatic temperature and a number of v_{O} , up to 1×10^5 MC trials are performed, including sets of trials for several MC random seeds, and the frequency of occurrence of a particular configuration characterized by a specific group of locations for the vacancies and with a specific local magnetic ordering is translated to the probability P_k , which is normalized over all the possible arrangements such that $\sum_k P_k = 1$. The average magnetization $\langle M \rangle_k$ of each configuration k is addressed by using the Fe magnetic moments predicted by the hybrid-DFT model for each $V_{a,p,d(1,2)}$ type within the arrangement. The final magnetization for the deficient perovskite, for a given oxygen deficiency, is then calculated as:

$$\langle M \rangle = \sum_k P_k \langle M \rangle_k \quad (1)$$

Equation 1 uses a distribution that is obtained by sampling according to a stationary Markov process, i.e., the occurrence of a configuration with a certain number of vacancies depends on the probability of occurrence of a particular configuration with one less vacancy.

Magnetic orderings used in the MC simulations are bound to the spin-polarization and supercell v_{O} -density modeled through DFT, which in this case means scenarios where magnetism is dominated by collinear cation interactions, one v_{O} /Fe-Fe pair approximately, as well as bath-temperatures for $k_b T$ below the formation energies and spin-gaps (energy difference between FM to AFM local ordering). Further aspects of our MC modeling are discussed in the following sections as well as in the appendices. We will show that the aforementioned approximations provide a

powerful representation of one of the most important properties of a perovskite intrinsic magnet i.e., its saturation magnetization, allowing a better understanding of the role of the v_{O} -density determined by the oxide synthesis process parameters.

Finally, we used the Interface Reaction of The Materials Project⁶³ to examine the magnetism of compounds resulting from the reaction of two STO-based perovskites in contact at an interface⁶⁴. The oxygen partial pressure and/or possible temperature effects are modeled by using a single chemical potential variable^{63,64}. The predictor provides us with the magnetic components' chemical fractions, which are then used to estimate the average magnetic moment⁶⁴ using the Materials Project database for the electronic properties of those components, and compared with our MC results and experiments.

3 DFT Results

3.1 Stoichiometric STF: $\text{SrTi}_{0.875}\text{Fe}_{0.125}\text{O}_3$

In "stoichiometric" STF ($\delta = 0$) the Fe ion would take a 4+ valence state to maintain charge balance. This valence state is present e.g., in STF synthesized at high oxygen pressures > 1 atm⁶⁵. Table 1 displays the energy characterization of STF as stabilized in high and low valence spin-states for $x = 0.125$. It can be seen that the high spin in Fe (corresponding to a (t_{2g}^3, e_g^1) $3d$ occupation) is preferred over the low (t_{2g}^4, e_g^0) case. Low band-gap/semimetallic Fe/Co-based compounds are usually expected to be found in low spin states e.g., well known oxides such as magnetite Fe_3O_4 or SCO itself. However, in magnetite, Fe valence is strongly affected by electron exchange between the tetrahedral and octahedral sites increasing the Fe-spin to an intermediate value⁶⁶, while in the case of O-deficient SCO, an intermediate Co spin is favored by Co-Vacancy-Co coupling through the AFM

Table 1 $\text{Sr}^{2+}\text{Ti}_{0.875}^{4+}\text{Fe}_{0.125}^{4+}\text{O}_3^{-}$ (HSE06) lattice parameter, Fe magnetic moment and energies corresponding high/low spin initializations.

d' (Å)	S_i	μ_B/Fe	E_{S_i} (meV/f.u.)
7.81	h	3.73	0.0 _{gs}
7.79	l	1.98	68.2

shared electrons³⁴. STF has a ~ 0.4 eV band-gap, as can be seen in Figure 2, which is bounded by the Fe- e_g^1 acceptor-like state, with a high spin preference deviating from the simplest molecular predictions.

This high spin seems robust with respect to tetragonal distortions, which are among the first factors lowering the crystal symmetry due to, e.g., substrate mismatch. As shown in Figure 3, large strains are needed to promote $10Dq$ changes. This last figure shows a high-to-low spin transition at $\sim 1.5\%$ in-plane strain. However, in order to capture such magnetic changes the relaxations have been constrained such that the perovskite single-crystal volume is conserved, e.g., in STC where the substrate-mediated strain is balanced with chemical strain due to Co incorporation⁴⁹. Fully relaxed strain always leads to similar high-versus-low initialized magnetic results, and magnetic constrains resolve the energy landscapes in favor of high spins too, as Figure A.1 shows. The ineffectiveness of these distortions is in accordance with Moreno et al.⁶⁷, which suggested that metal-ligand distances are not so decisive in both the intrinsic e_g splitting and cubic field splitting $10Dq$. Bonding with deep 2s (free atom) orbitals, rather than shallow 2p ones, are essential to change orbital occupations^{36,67}.

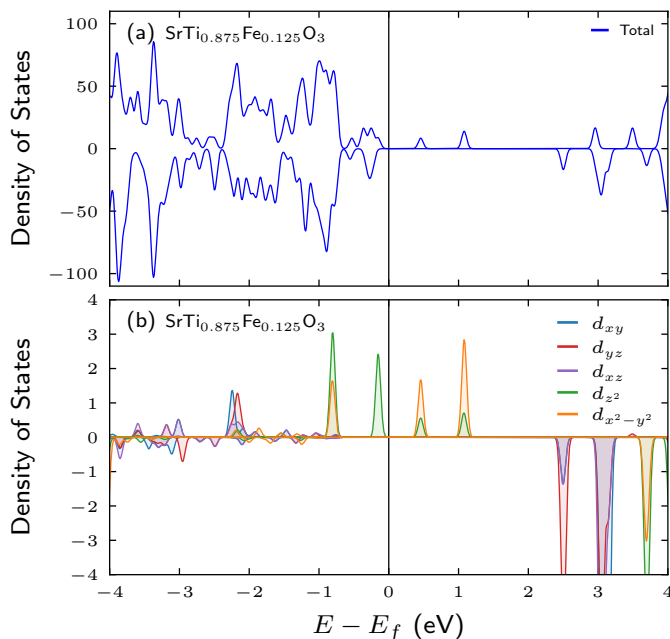


Fig. 2 (a) Total Density of States (DOS) and (b) Fe ion d -orbitals projected DOS for $\text{SrTi}_{0.875}\text{Fe}_{0.125}\text{O}_3$.

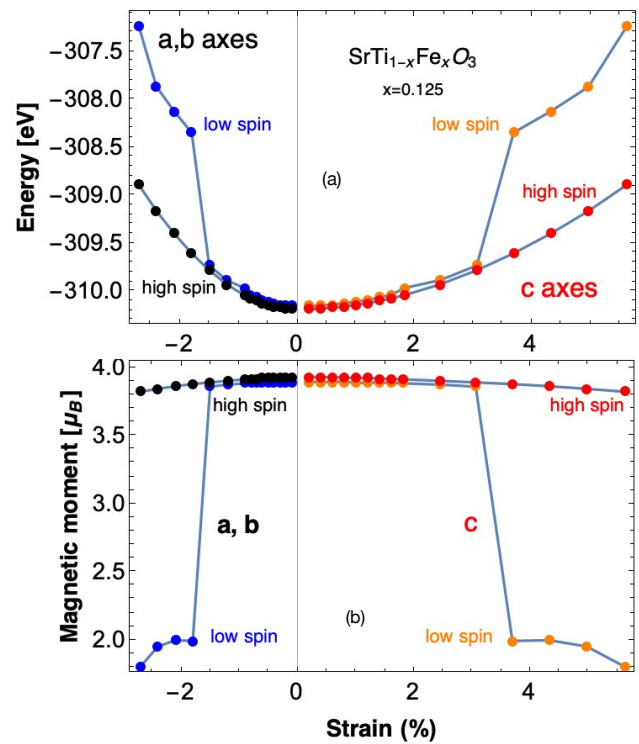


Fig. 3 (a) Energy and (b) magnetic moment of STF with $x = 0.125$ and $\delta = 0$, for several tetragonal strains: in the relaxations (GGA+U) Fe are initialized with Fe^{4+} low and high spin states. Black/blue curves correspond to the tetragonal (a, b) axes while red/orange correspond to the out-of-plane c axis.

3.2 Stoichiometric STF: $\text{SrTi}_{0.75}\text{Fe}_{0.25}\text{O}_3$

We focus from this point onward on the composition corresponding to $x = 0.25$, which within our model perovskite means two Fe/u.c., as Figure 1 shows. These Fe cations can be arranged into three different distributions, which we considered and evaluated at high and low spin states for the corresponding valences and ferromagnetic/antiferromagnetic local spin orderings. In Table 2 hybrid relaxation results are presented, where $E_{(h,l)}^{FM/AFM}$ describes the energy difference of the specific state with respect to the global ground state. $nm_{\text{Fe},i,f}/a$ and $S_{i,f}$ are the initial and final Fe-Fe supercell distances and local magnetic moments, respectively. We select for each Fe distribution the lowest energy state, i.e. the global ground state corresponding to the ferromagnetic $E_{h_{FM}}$ high-spin ordering. The first two major findings from Table 2, which already differ qualitatively from what happens for instance in STC³⁴ are: the magnetic cations are stabilized preferably at a first nm_{Fe} configuration with respect to the B-B (ABO_3) possibilities, Figure 1(a); and high spin states dominate the stabilized magnetism, which follows the conclusions of the previous section.

In Table 2 the energies of the low spin states that are comparable to those of high spin states are due to self-consistent switching to high spins. Limiting the model to force those low-spin states to be present leads to higher energies as already shown by Figure 3 and other results in Table 2, with energies over ~ 150 meV in

this last case. Comparatively, the intermediate distance between the Fe ions allows an AFM ordering, while in STC it stabilizes the ground state in a FM configuration. In this $\delta = 0$ case, it is energetically less expensive to arrange the Fe in an AFM ordering by switching one of the two spins than by stabilizing larger nm_{Fe} . The $E_{h_{\text{AFM}}}$ energy increases as nm_{Fe}/a increases while keeping AFM local moments, however, if the local moments are kept FM the system seems to experience an instability when Fe ions are pulled apart. They stabilize the same in whatever location they are placed, not without a huge energetic cost from the ground state. The results in Table 2 therefore demonstrate the differences in exchange-coupling between the Fe ions in these three configurations i.e., the oxygen mediates magnetic interactions through super-exchange mechanisms that in this case of Fe-substitution seem negligible beyond first nearest-neighbors.

Our results for stoichiometric STF in Table 2 therefore suggest that in a physical sample of STF, a mixture of FM and AFM local orderings would be stabilized giving rise to an average magnetization made up of contributions from various Fe configurations. However, the $[1,0,0]$ arrangement of Fe-cations and its magnetic contribution would be statistically preponderant compared to other configurations.

3.3 Oxygen deficient STF: $\text{SrTi}_{0.75}\text{Fe}_{0.25}\text{O}_{2.875}$

For STF, the magnetization as a function of the oxygen pressure during growth was described in References^{13,33}, in which a maximum magnetization is reached at some ν_o density. In this final DFT section, we analyze the magnetic behavior of STF for $x = 0.25$ and $\delta = 0.125$ i.e., one vacancy/supercell. This analysis helps in interpreting the experimental behavior and provides a basis for more complex or computationally demanding descriptions.

Figure 1 shows the five different vacancies that are found to be symmetrically irreducible for all the Fe-Fe cation configurations, according to our considerations in Section 2. In Table A.1 we summarized all the results for $nm_{\text{Fe}_i}/a \sim 1$, in which FM and AFM states have been relaxed for the valence states corresponding to a neutral formula unit. The sub-indices a_1 or a_2 label the vacancies according to Figure 1. We can see that both a_1 and a_2 gs are given by AFM states with what seem to be high Fe spins. These two systems have vacancies coordinating a Fe ion, but they present different resulting structures i.e., a tetragonal and an orthorhombic-like structure, respectively. The Fe- ν_o -Fe

configuration reduces the symmetry of the system less, making it the global ground state among competing a_1^{gs} and a_2^{gs} as Table A.1 shows. This is also reflected in the magnetic moments, where we see in a_2^{gs} two slightly unequal moments differing by $\sim 0.1\mu_B$, which is a consequence of the different hybridized $3d$ -Fe occupations displayed in Figure 4. This last figure shows the total and $t_{2g}e_g$ densities of states for the gs in the stoichiometric and $a_{1,2}$ deficient cases. For $\delta = 0$, the system is FM and both spins are in similar states with polarized seemingly half-filled $t_{2g}e_g$, which would correspond to a $t_{2g}^3 e_g^1$ occupancy for Fe_h^{4+} spin states. In a_1^{gs} , Fe cations are AFM ordered and in similar states, i.e., an occupancy close to a $t_{2g}^4 e_g^2$ for Fe_h^{2+} spin states. When checking a_2^{gs} in Figure 4, we find the solution is associated with a mixture of valence spin states, for an AFM ordering, which agrees with the reported ferrimagnetic-like behavior found in STF¹³: the Fe ion that lies in the incomplete O_5 octahedra, here called Fe_2 , seems to have an electronic distribution characteristic of a hybridized $t_{2g}^3 e_g^2$ for a Fe_h^{3+} character and therefore larger local magnetic moment than Fe_1 , which resembles the Fe state in the previous cases.

One solution for V_{a_1} has zero net magnetization, while a second one V_{a_2} , has a small magnetization. One can already intuit that one way of increasing or decreasing the perovskite magnetization is to let the system stabilize different arrangements of ν_o . The two vacancies $V_{a_{1,2}}$ have spin-gaps between FM and AFM states, just below a few dozen meV, which one could imagine competing with a room temperature thermal excitation.

We now describe briefly the rest of the ν_o considered here. Tables A.2 and A.3 present the characterization of the $[1,1,0]$ (plane) and $[1,1,1]$ (diagonal) arrangements, respectively. The first one displays the results corresponding to V_{p_1} and V_{p_2} in Figure 1. In this cation distribution the AFM and FM stabilized solutions are energetically close, as the gs for $V_{p_{1,2}}$, both AFM, are within just a couple of meV of the closest FM state, which also presents high spin occupation. In both cases, the vacancy coordinates one Fe ion, and therefore one of the Fe magnetic moments is always larger than the other one, in a similar manner to the behavior of Co observed in STC³⁴. In this last case, though, the difference is due to a low-to-high spin state transition, while in STF it originates from hybridization between high Fe^{4+} and Fe^{3+} states as Figure 5 suggests. Hence, the system relaxes to a magnetized state, either a ferrimagnetic ordering with $\sim 0.05\mu_B/\text{Fe}$ or a FM one with $\sim 4.16\mu_B/\text{Fe}$, respectively. The energy difference between these orderings seems independent of the V_p type as well as the local Fe magnetic moments.

Although here we are interested in evaluating the magnetization, and V_{p_1} and V_{p_2} behave similarly from that viewpoint, among those two ν_o the first one turns out to be more interesting for multiferroic purposes. Its $3d$ hybridization is slightly shifted just below E_f and the system is a semiconductor with a 2.15 eV band-gap, which is adequate for maintaining a ferroelectric polarization, as discussed for STFC⁶. This work showed how oxygen migration and oxygen deficiency modulate the band-gap and electric polarization in Fe, Co-substituted STO with defects

Table 2 $\text{Sr}^{2+}\text{Ti}_{1-x}^{4+}\text{Fe}_x^{4+}\text{O}_3^{2-}$ properties for $x = 0.25$ (HSE06).

E_{S_i} (meV/f.u.) for configurations in Fig. 1 with S_i				
nm_{Fe_i}/a	$E_{h_{\text{AFM}}}$	$E_{h_{\text{FM}}}$	$E_{l_{\text{AFM}}}$	$E_{l_{\text{FM}}}$
1	32.5	0.0 _a	33.6	201.0
$\sqrt{2}$	35.7 _b	37.5	158.1	157.3
$\sqrt{3}$	37.2	36.4 _c	36.3	167.6
Lattice parameters and magnetic structure for a, b, c				
$S_f^{1,2}$ (μ_B)	(a', b', c') (\AA)	V (\AA^3)	nm_{Fe_f}/a	E_{bg} (eV)
$(3.7, 3.7)_a$	$(7.80, 7.80, 7.79)$	474.66	~ 0.89	0.00
$(3.7, -3.7)_b$	$(7.80, 7.80, 7.80)$	474.70	$\sim 0.9\sqrt{2}$	0.01
$(3.7, 3.7)_c$	$(7.80, 7.80, 7.80)$	474.69	$\sim 0.9\sqrt{3}$	0.16

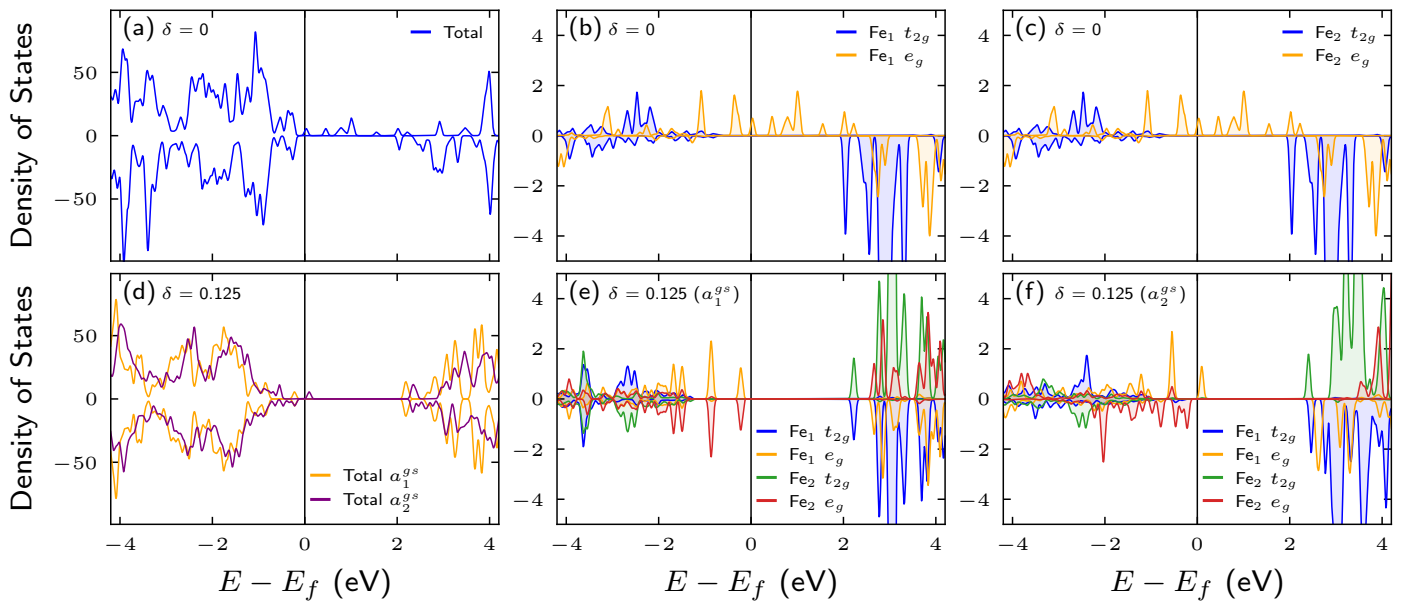


Fig. 4 (a) Total DOS and (b, c) $t_{2g}e_g$ -projected DOS of Fe_1 and Fe_2 for the ground state stoichiometric STF. (d) Total DOS and (e, f) $t_{2g}e_g$ -projected DOS of Fe ions for the $V_{a_{1,2}}$ vacancies ground states in $SrTi_{0.75}Fe_{0.25}O_{2.875}$.

such as the ones studied here.

Figure 5 shows the total and projected density of states for V_{p_1} . It is clear that the system is AFM and that different $3d$ -occupancy determines the magnetism of the solid solution, in spite of the close local spin values. One Fe is stabilized as $t_{2g}^3 e_g^1$ while the other one is $t_{2g}^4 e_g^2$. The subtle but consistent up-down population in one of the two t_{2g} orbitals (Fe_2) of the ground states in Table A.2, which is also present in several of the less stable ground states, differentiates the two magnetic states of the Fe ions sufficiently as to have a ferrimagnetic moment in the supercell.

We now analyze V_{d_1} in Figure 1. Table A.3 shows that in this configuration the system stabilizes an AFM ordering. There is a FM solution (d_1^{ss1}) within a very narrow energy difference, which is a repercussion of the large $nm_{Fe_i}/a \sim \sqrt{3}$ distance compared to an O-mediated nm_{Fe} super-exchange. Fe ions are coordinated by completed octahedra in two crystallographic directions other than $[100]$, creating a tetragonal-pyramid chemical strain that slightly favors indirect antiferromagnetism, in accordance with a quasi-static d^4-d^6 180° bond according to Goodenough³². The second lowest energy state is also AFM though it is not equivalent to d_1^{ss} . The slightly compact packaging of ss_1 promotes a shifting of the e_g in Figure 5 which creates available hybridized states that prevent a band-gap. The magnetic moments are given by high spin states following the behavior exhibited by $V_{p_{1,2}}$, which stabilized $t_{2g}^3 e_g^1$ and $t_{2g}^4 e_g^2$ spin states, with the vacancy surrounding the first one (Fe_1). Also, d_1^{ss} has a band-gap of 2.04 eV, which is larger than the one for the V_p case but not necessarily larger than the one for V_{a_1} . This indicates that proximity of the cations is not a predominant factor in the metallic-like behavior due to cluster formation in perovskite solid solutions of this kind when we consider v_o . For instance, in semi-metallic SCO a gap opens up and

increases with δ while perovskites such as Fe, Co-substituted STO present a maximum gap at intermediate vacancy density⁶ for different cation nm distances.

4 Monte Carlo Results

We are interested in implementing a model that could give us further insights into the dependence of magnetization on the number of vacancies. In this section, we describe the results of the Monte Carlo approach described in Section 2. Among all the v_o results in Tables A.1, A.2 and A.3, we selected a group of vacancies that represent an STF solution with the same arrangement of magnetic cations. The supercells in Figure 1 give rise to STF crystals with just one of three Fe-Fe arrangements; therefore, if the ab-initio energies are approached as statistical weights, those would meaningfully represent a long range ordered crystal i.e., there is no mixture of $[1, 0, 0]$, $[1, 1, 0]$ and/or $[1, 1, 1]$ arrangements of Fe-Fe magnetic pairs.

To check which vacancies are energetically favorable in each configuration, we calculate the formation energy E_f^δ for the gs and ss of each $V_{a,p,d}$. Table 3 gives the formation energy E_f^δ of oxygen vacancies as calculated with Equation 2:

$$E_f^\delta = E_\delta - E_{\delta=0} + \mu_O \quad (2)$$

where E_δ is the total energy of the crystal with one oxygen vacancy after relaxation, and $E_{\delta=0}$ is the total energy of the stoichiometric crystal ($\delta = 0$) with the corresponding Fe-Fe pair orientation. μ_O is the chemical potential of O, calculated as half the energy of an isolated O_2 molecule⁶⁸.

In the case of V_{d_1} we have used ss_2 , as ss_1 and gs converged to the same magnetic state, and because ss_2 is FM as opposed to gs , which happens with the gs and ss for $V_{a,p}$ too. Table 3 confirms that the diagonal configuration places the Fe ions too

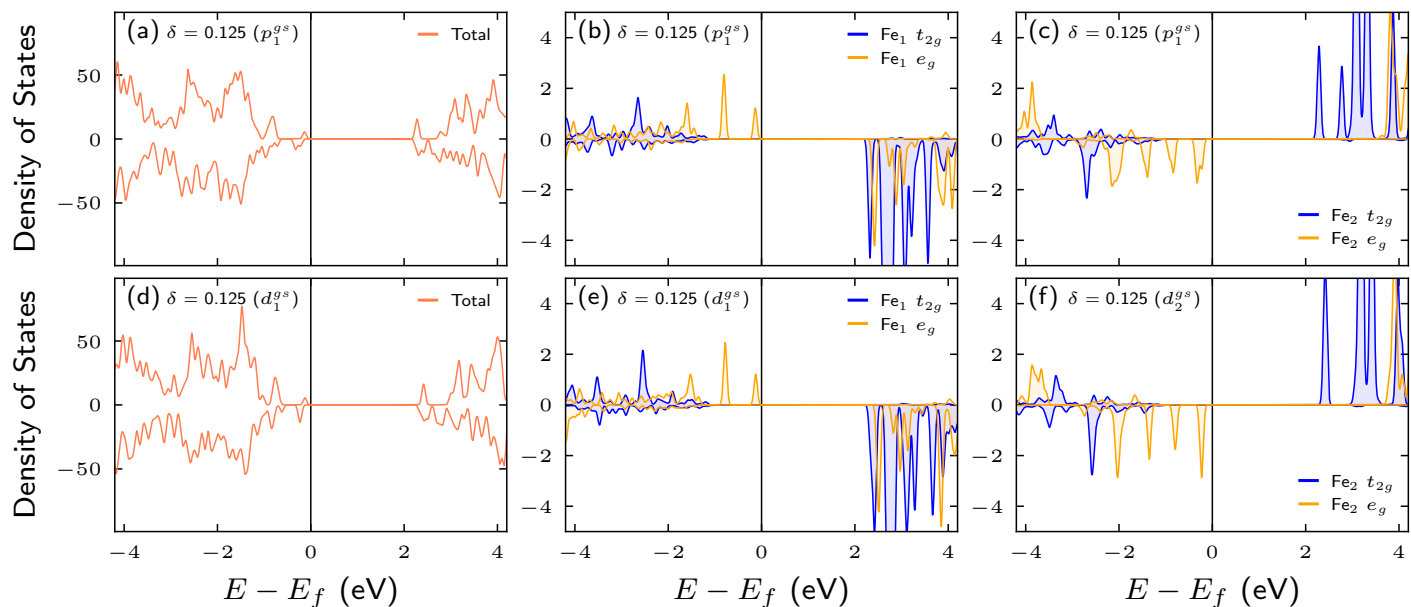


Fig. 5 (a) Total DOS and (b, c) $t_{2g}e_g$ -projected DOS of Fe ions for the V_{p1} vacancy ground state in $\text{SrTi}_{0.75}\text{Fe}_{0.25}\text{O}_{2.875}$. (d) Total DOS and (e, f) $t_{2g}e_g$ -projected DOS of Fe ions for the V_{d1} vacancy ground state in $\text{SrTi}_{0.75}\text{Fe}_{0.25}\text{O}_{2.875}$.

Table 3 v_o formation energies E_f^δ and space group (SG) symmetry for gs/ss in Tables A.1, A.2 and A.3 (HSE06).

E_f^δ (eV)	V_{a1}	V_{a2}	V_{p1}	V_{p2}	V_{d1}
gs	3.74	4.21	3.94	3.90	3.92
ss	3.98	4.40	3.95	3.91	3.92
SG	P4/mmm	Pmm2	P4mm	Pmm2	P4mm

far for them to sense the change of the magnetic coupling and/or slight tetragonal distortions; therefore, we have practically energy-equivalent vacancies for this configuration. Creating these last v_o is cheaper than creating V_{p1} but slightly more expensive than V_{p2} , which is a consequence of the in-plane structural changes due to the $[1, 1, 0]$ Fe-ion arrangement that are competing with the Ti- v_o -Fe chemical strain caused by V_{p2} ³⁴, as symmetry in Table 3 indicates. Among all v_o in Table 3, V_{a1} is energetically cheaper to create and V_{a2} is comparably more expensive. Nevertheless, the $[1, 0, 0]$ Fe-Fe $\delta = 0$ configurations are cheaper overall when revisiting Table 2. Moreover, V_{a1} and V_{a2} can be connected by adiabatic oxygen migration path that promotes ferroic orders⁶. Experimentally there is a difference between the in-plane and the out-of-plane magnetization in STF, which is related to the influence of magnetoelastic effects and the formation of columnar structures within the perovskite matrix, orienting the overall direction of the magnetization¹³. These previous observations suggest that we consider the vertical Fe-Fe configuration as well as with the energy results in Table A.1 as a reasonable representative STF configurational space to be sampled by our Monte Carlo modeling.

We then created vacancies in a $[1, 0, 0]$ Fe-Fe oriented MC model-crystal starting from a $\delta = 0$. While increasing the number of vacancies such that δ ranges from 0.0 to 0.125 (this corresponds to a maximum of the magnetization for $\text{SrTi}_{1-x}\text{Fe}_x\text{O}_3$

with $x = 0.25$ ^{6,34,36}), we apply two constraints: (i) v_o can take either a V_{a1} or a V_{a2} character/location by bearing the gs/ss corresponding energies, associated Fe magnetic moments and corresponding Fe-Fe alignments predicted by our DFT models; (ii) interactions between vertically aligned pairs of magnetic cations, separated at least by $2a'$, are negligible. Vacancy interactions as well as charging effects due to these defects are also likely to be negligible as suggested by this and other ab-initio modelling³⁶. Finally, we run Monte Carlo simulations by adding O-vacancies while following the algorithm illustrated in Figure A.3 and the description in Section 2. From the stochastic method, frequencies of specific vacancy-configurations are obtained, which are then translated to normalized probabilities to be used in Equation 1.

Figure 6 displays the modeled magnetization results in the absence of a magnetic field for oxygen-deficient STF. For all the adiabatic bath temperatures simulated here the magnetization has a similar behavior i.e., it increases linearly from low values $\sim 0.05 - 0.1\mu_B$, smoothly reaching a maximum of $\sim 0.35\mu_B$ at intermediate oxygen deficiency $\sim \delta = 0.093$ ($\sim 6 v_o$); then, if v_o keeps increasing, the magnetization slowly decreases but with a reduced linear slope compared to that below the maximum. To compare our intuitive model with experiments, we have extracted the remanence ($H=0$ kOe) and saturation magnetization ($H=10$ kOe) from the room temperature STF hysteresis loops reported in Goto et al.¹³. Figure 7 displays the magnetization vs. oxygen pressure during deposition.

Figure 7 shows a good agreement of the STF magnetization trend predicted by Figure 6 and the experimental results. In fact, although the relation between the number/density of vacancies and the oxygen pressure during deposition in these kind of

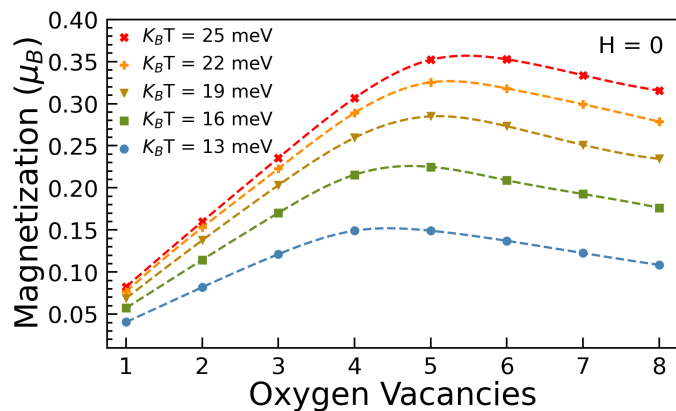


Fig. 6 DFT based Monte Carlo modeling of oxygen deficient STF ($x = 0.25$) magnetization for different number of v_o . Figure A.3 displays the MC scheme implemented to get these magnetizations.

experiments is still an open question and several models have been proposed^{6,65}, what is clear is that high oxygen pressures during growth lead to a lower content of oxygen vacancies, and low pressures give rise to large content of v_o . Therefore, Figures 6 and Figure 7 should be read such that the linear behavior below $\sim 5-6 v_o$ in the modeling results, which have a higher slope, correspond to the linear behavior for high pressure in the experimental results, which also is the linear part with the higher slope. The slow decrease of the magnetization in the model when there are more vacancies also represents well the slower experimental decrease of the magnetization, and the threshold given by the saturation magnetization at room temperature (~ 25 meV) is also captured.

To the best of the author's knowledge there are not models that accurately provide the number of oxygen defects for a given oxygen pressure yet, however, a logarithmic relation has been used e.g., between the oxygen deficiency δ' and the oxygen pressure⁶⁵. If we use the experimental results in Kuhn et al. work's for nonstoichiometric STF at the lowest reported temperature⁶⁵, such a pressure/ δ' (for $\log(pO_2)$) map suggests that the magnetization peaks in Figure 7 are given for oxygen-deficiency values that in our perovskite model would traduce to slightly less δ than that corresponding to $4 v_o$; our simulations displayed in Figure 6 show peaks of magnetization at $\sim 4-5 v_o$. One possible reason for this difference is that the experimental Fe content, $x = 0.35$, is lower than the model composition. The oxygen content is given by $3 - x/2 + \delta'$ in Kuhn et al.⁶⁵ so there is less deficiency δ for $x = 0.35$. The model also corresponds to a higher temperature than the experiment, which was measured at room temperature. In Figure 6 we showed that the location of the representative maximum of magnetization can be shifted when the temperature is changed. For a given number of vacancies the magnetization decreases if the temperature decreases.

The ability of our MC simulations to reproduce these experimental characteristics is based on the fact that a great portion of the effects observed in Figures 7 is due to bulk-like magnetic

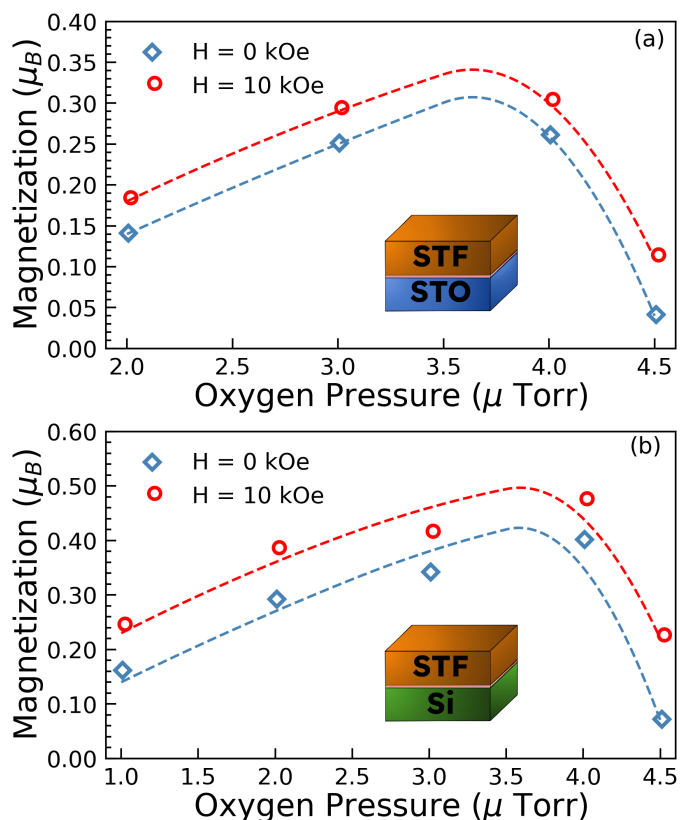


Fig. 7 Experimental out-of-plane magnetization for oxygen deficient STF films deposited on (a) STO; (b) Si. Selected data reproduced from Goto et al.¹³ for remanence and saturation magnetizations. Dashed lines are interpolating guiding lines.

orderings that are thermally activated. In Figure 8 we have displayed the distribution of the probabilities for the occurrence of a specific number of $V_{a_{1,2}}$ when the temperature is modified. These last figures show that while for low temperatures V_{a_2} is less likely, for room-temperature its probability has increased and therefore the probability of having a nonzero magnetization has also increased, because V_{a_2} has finite magnetization for either FM and AFM polarization; FM ordering increases the magnetization more, but it comes with higher energetic price. When the number of vacancies increases the probability of having fewer V_{a_1} and more V_{a_2} increases for a given temperature. This is also because of a topological factor that is rather difficult to measure microscopically i.e., there are more $Ti-V_{a_2}-Fe$ possible sites than $Fe-V_{a_1}-Fe$ ones. So, as the bars in Figure 8 suggest, when there are more possible vacancy sites than actual vacancies and the temperature is low the magnetization increases until a roughly even distribution between $a_{1,2} gs$ is established. Once the number of vacancies competes with the available sites the contribution from a_1 does not increase further while a_2 provides mainly antiferromagnetic contributions that also decrease the magnetization. If the temperature increases, it promotes the formation of new V_{a_2} rather than gs to ss transitions in V_a as the lower panel in Figure 8 shows, and for a sufficient number of vacancies the magnetization will decrease more due to a AFM versus FM competition within V_{a_2} orderings than to the

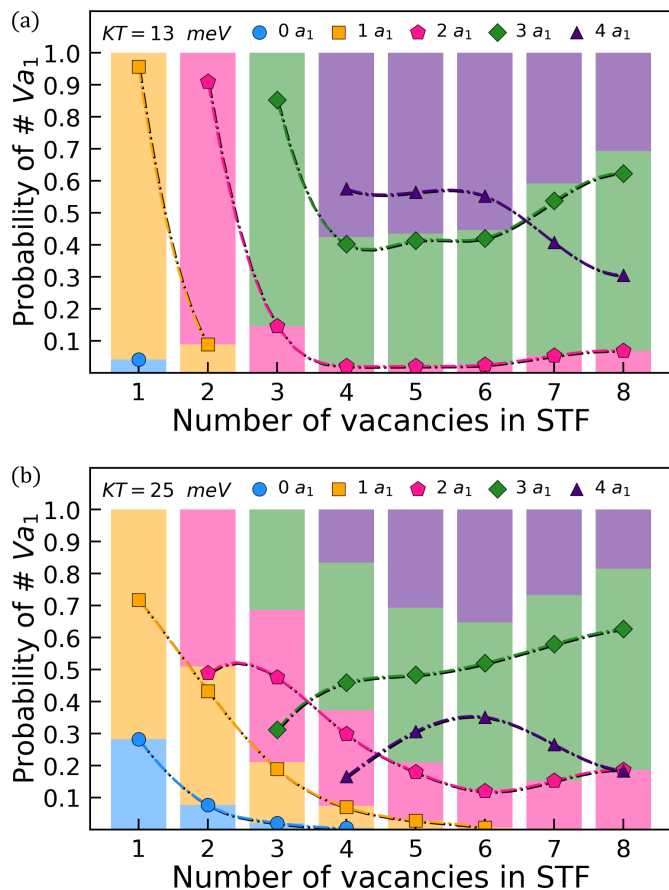


Fig. 8 Probability of occurrence of specific types of vacancies among V_{a1} and V_{a2} for a given δ and a bath temperature corresponding to $k_b T$ e.g., 13 meV (a), and 25 meV (b). For the sake of simplicity, as $P(l)_{V_{a1}} + P(n)_{V_{a2}} = 1$, it is normalized for $(l+n) = \#$ of $v_o \Rightarrow \delta$, we plot just $P(l)_{V_{a1}}$ such that the probability $P(l)_{V_{a1}} \rightarrow$ (symbol) $l a_1$. We have alternatively used in the background %-bars of the same colors to illustrate the quantity of $l a_1$ that would result out of the total number trials in the MC simulations.

competition between the different types of v_o . The balance between what we could call “Fe-Fe magnetic defects” therefore dominates the magnetic properties in these systems.

We finally consider the effects of the interface between the perovskite and the substrate. Although a detailed study of this contribution is beyond the scope of this article, we can describe the effect of the composition of the STF at the interface. Figure 9 shows the averaged magnetic moments at the interface obtained as described in Section 2, by applying the Materials Project Interface Reaction^{58,63,64}. We simulate the STF/STO interface for three different interface compositions based on a combination of STO and STF with 50% Fe, chosen because most data is available in the Materials Project database for this composition. Figure 9 shows that the interface is able to stabilize low spin states, with intermediate values for the oxygen chemical potential able to promote mixed 3+ and 2+ Fe low spins for lower STF content. By increasing Fe content in STF, the system begins to recover the bulk-film behavior, with 4+ low-spin occupancy being favored. Therefore, the interface also contributes to the magnetization by

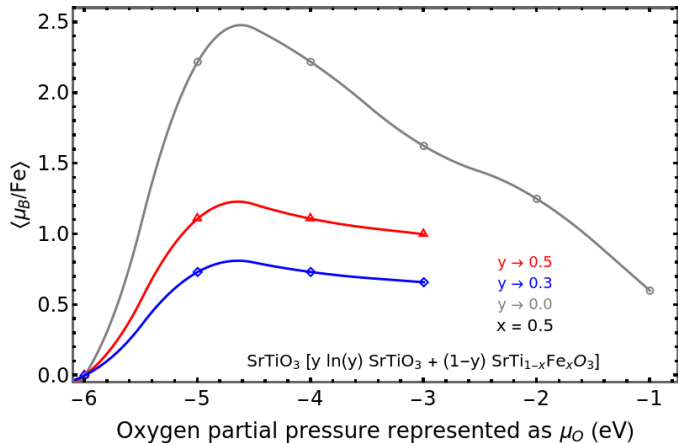


Fig. 9 Magnetism at STO/STF interface versus the oxygen-gas chemical potential μ_O . The averaged Fe magnetic moment at the interface was obtained by applying the Interface Reaction of the Materials Project^{58,63,64}. Solid colored lines are guiding lines.

tuning the Fe moments among low spin states, which range within $(0-2)\mu_B$. In fact, for large chemical potentials it is possible to find interface-compounds with magnetic contributions arising from Ti ions, which would be in accordance with recent studies in oxygen deficient STO and STF⁶ that found magnetic Ti sub-lattices in the perovskite.

5 Conclusions

We have performed Hybrid-DFT calculations, Monte Carlo simulations as well as interface reactions to model the magnetization in oxygen-deficient STF and compared the results with experimental data. We have shown that the experimental behavior is likely driven by three main factors: (i) competition between specific “magnetic defects” consisting of Fe cations that are coordinated by energetically different v_o , which give rise to different local spins and magnetic alignments. (ii) The distribution of Fe cations in relation to the density of v_o plays an important role in defining the oxygen pressure at which the rise in magnetization triggered by the AFM to FM local switching starts to be reversed by thermally activated magnetic defects which promote a ferrimagnetic character. (iii) The magnetic cations at the interface can present a variety of low spin states, in contrast to the high-spin dominated occupancy in the bulk material, which on average decreases the magnetic moment per Fe for both large and very low oxygen partial pressures.

A full magnetic simulation of this experimental situation would require a many-body Hamiltonian + ab-initio/Molecular dynamics modeling at finite temperature, in which the overwhelming number of ions/defects would require the microscopic parameters to be calculated self-consistently. It would also require very large supercells if we were to consider all the different configurations for the magnetic ions and vacancies in the structural relaxations, which would be computationally prohibitive even for some non-hybrid functionals. Faster semi-local/meta functionals would require us to constrain the systems to some stabilized valence spin states⁶⁹, while lacking the compromise between

magnetic and conductive properties of hybrids³⁶. Our approach on the other hand, is able to capture useful characteristics that can be used as fingerprints to synthesize new materials at an affordable computational cost, for instance, using this approach we could set constraint vectors in supervised Machine Learning-based simulations that use classically obtained configurational spaces^{70–72}.

The values presented here can be compared with other ab-initio methods, which could help to determine how to enrich the complexity of the configurational space so more experimental parameters can be accounted for or in turn, recent benchmarks for DFT on magnetic TM⁷³ could be discussed by considering oxygen stoichiometry as a variable. The realization of such benchmarks would also help to study the multiferroic character of these $\text{ABO}_{3-\delta}$ systems e.g., GGA+U and HSE06 both qualitatively agree on the t_{2g} - e_g orbital occupation of the Fe ions and its resulting high-spin magnetic moment, however, their predicted occupancy differ around the Fermi level as Figure A.2 displays. The partially filled GGA+U e_g orbitals at the Fermi level are resolved by the hybrid functional. Such splitting can be partially attributed to the mixing of Hartree-Fock exchange in HSE06, as already established in other TM perovskite⁷⁴, leading to an improved description of the electronic structure and therefore of the energy band-gap, which is crucial to qualify the ferroelectric behavior with modern theory of polarization⁵. Because of the modulating effect of the O-deficiency on the band-gap³⁶, a wider scope including non-stoichiometry systems seems necessary. Also, from the Hamiltonian modeling viewpoint, using a unique ground-state configuration from Table A.1 would lead us to an orbital-theory-like approximation without a distribution of valences and oversimplifying the magnetism respect the oxygen deficiency. In contrast, it would require considering a complex fermionic model to account for the change of Fe 3d occupancy if several exchange interactions are fixed as constraints in a Hamiltonian with a varying number of particles per site. In our intuitive Monte Carlo method, we can consider microscopic information for several configurations of the vacancy-(Fe/Ti) defects, and in this case the stochastic method samples the vacancy configuration space created by different vacancies, considering the possible associated magnetic polarizations for their respective neighboring Fe ions. Moreover, in ABO_3 systems such as STFC⁶ has been recently shown that if larger deficiencies are considered and oxygen migration can be activated, the magnetism originated on the Ti ions as well as the oxygen magnetic moments could become relevant. In Table A.4 we can already observe how ground-state solutions energetically less favorable than those used to obtain Figure 6 possess tiny but larger (O,Ti)-sub-lattices moments than those at V_a configurations.

Also, while a good discrimination between FM and AFM stable/meta-stable states in $\text{ABO}_{3-\delta}$ ferroic oxides is not always trivial to achieve from DFT and challenges such as the so-called spin-contamination^{75–77} could be of interest in nanosized multiferroics^{2,5}, within our scope of optimizing the oxygen stoichiometry to maximize the spontaneous magnetization different adiabatic paths with different cations/defects topology

could be interpolated looking for stable solutions as well as different crystal structures among the solid solutions with the same O-stoichiometry could be researched; the frequency of the vacancy formation could also be used through structural effects as it could be the crystalline/magneto-elastic anisotropies, which would allow us to use the saturation magnetization as a close fingerprint of such magnetization value as Figure 7 suggests.

Our model provides guidelines for predicting magnetization in complex oxides with point defects, which is relevant for developing materials for data storage and data processing, permanent magnets, or multiferroic materials. Moreover, this investigation provides hints about the type of crystal symmetry that should be targeted as well as the relationship between oxygen content and saturation magnetization.

Conflicts of interest

The authors declare no conflict of interest.

Acknowledgements

J.M. Florez and E. S. Morell acknowledge financial support of project FONDECYT Regular 1221301, Agencia Nacional de Investigación y Desarrollo (ANID), Chile. M.A. Solis acknowledges financial support of USM-DPP, Chile. C.A. Ross acknowledges National Science Foundation: DMR 1419807.

J.M. Florez also thanks Prof. Shyue P. Ong from the Department of NanoEngineering at the University of California, San Diego, for helpful discussions about the Materials Project tools for modeling oxygen-deficient perovskites. The authors also thank M. A. Opazo for helpful discussions about TM-substituted SrTiO_3 magnetic properties.

A Appendix

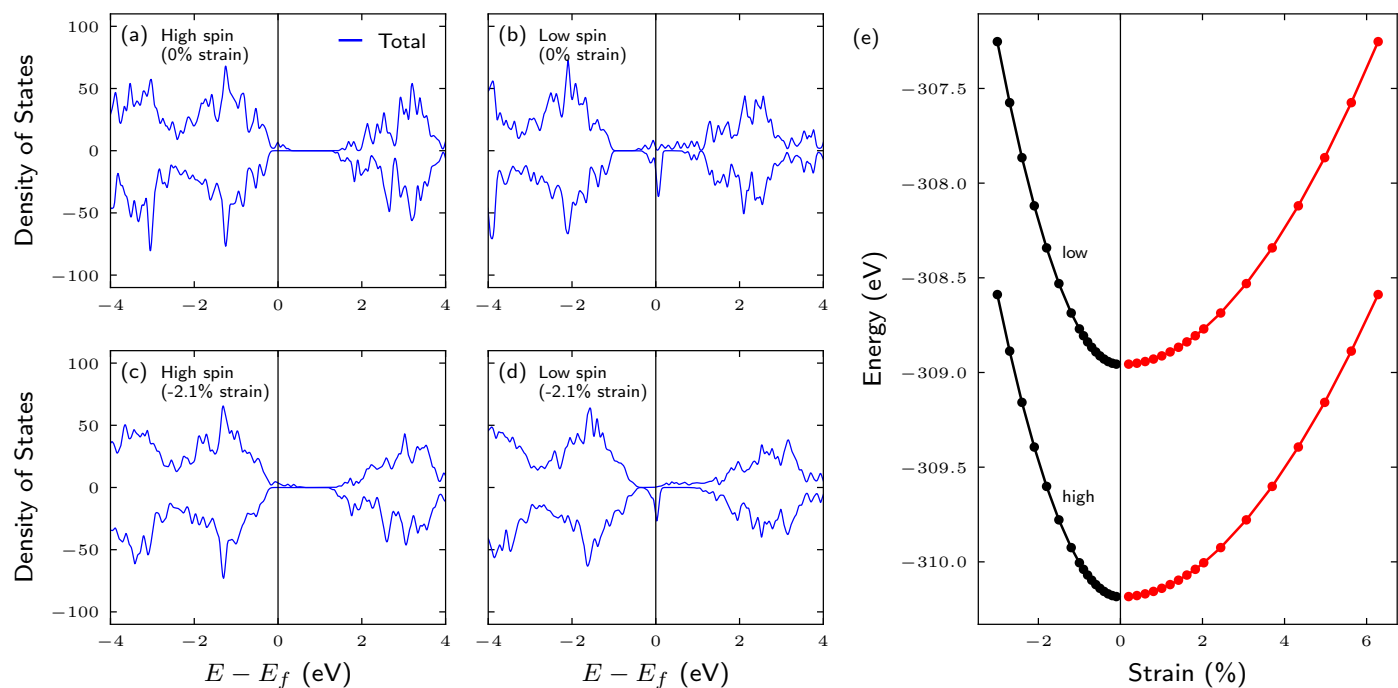
A.1 STF for $\delta = 0$ and $x = 0.125$ 

Fig. A.1 Total DOS (a-d) and energy (e) of STF with $x = 0.125$ and $\delta = 0$ under strain (GGA+U). High and low spin state energies (e) were obtained by constraining the magnetism of the supercell accordingly. The DOS are calculated for zero (a,b) and 2.1% tetragonal strain (c,d).

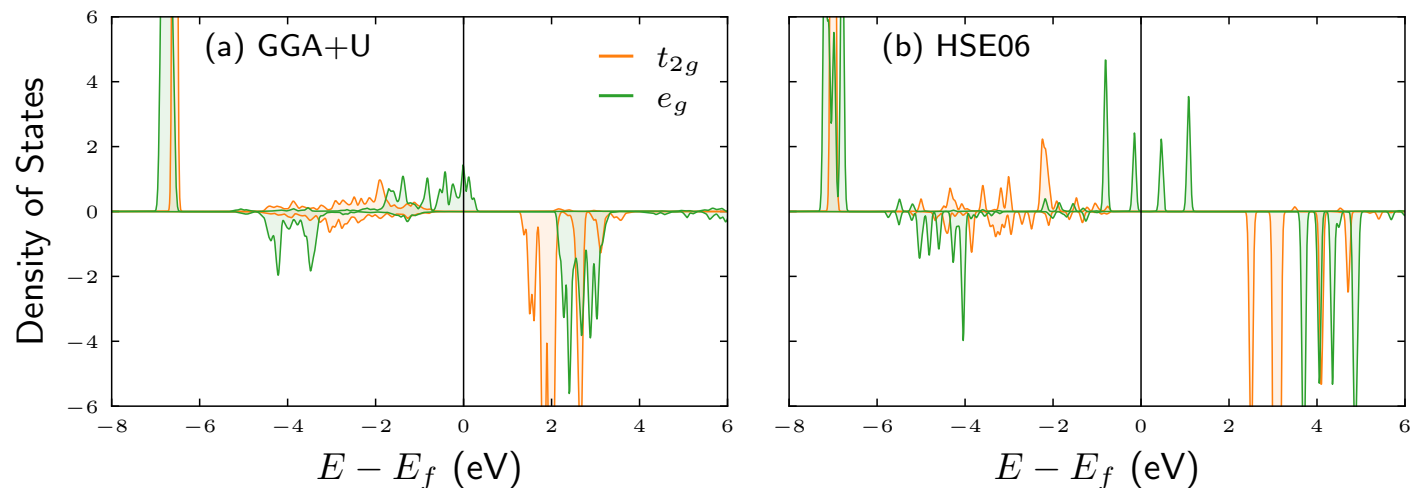


Fig. A.2 (a) GGA+U and (b) HSE06 Fe ion t_{2g} - e_g projected DOS for STF with $x = 0.125$ and $\delta = 0$ without strain.

A.2 STF for $\delta = 0.125$ and $x = 0.25$ Table A.1 $\text{Sr}^{2+}\text{Ti}_{0.75}^{4+}\text{Fe}_{0.25}^y\text{O}_{2.875}^{2-}$ properties for vacancies \mathbf{V}_{a_1} and \mathbf{V}_{a_2} (HSE06). FM and AFM energies of $nm_{\text{Fe}} \sim a'$ configurations for each initial $S_i^{1,2}$ Fe spins, as well as lattice parameters, magnetic structure, band-gap and relative energy of the selected gs and ss states.

y	$S_i^{1,2}$	\mathbf{V}_{a_1}		\mathbf{V}_{a_2}	
		E_{FM} (meV/f.u.)	E_{AFM} (meV/f.u.)	E_{FM} (meV/f.u.)	E_{AFM} (meV/f.u.)
(2+,4+)	h,h	248.3	— _{gs}	98.9	0.02
	h,l	222.5	107.9	223.7	134.9
	l,h	236.1	233.7	206.6	197.6
	l,l	108.3	108.4	78.8	135.3
(4+,2+)	h,l	238.1	232.8	197.6	197.5
	l,h	222.8	107.9	234.8	135.6
	l,l	107.9	108.0	135.2	135.2
(3+,3+)	h,h	31.2 _{ss}	0.06	23.8 _{ss}	— _{gs}
	h,l	313.3	234.8	268.6	197.4
	l,h	313.3	233.3	196.9	197.6
	l,l	447.9	218.2	408.3	0.02
State	$S_f^{1,2}(\mu_B)$	$(a', b', c') (\text{Å})$	$V (\text{Å}^3)$	E_{bg} (eV)	$\Delta E_{a_i^{gs}}$ (meV/f.u.)
a_1^{gs}	(4.07, -4.07)	(7.82, 7.82, 7.83)	479.33	2.15	—
a_1^{ss}	(4.14, 4.14)	(7.82, 7.82, 7.84)	479.65	0	31.2
a_2^{gs}	(4.07, -4.17)	(7.83, 7.85, 7.83)	481.48	0	59.6
a_2^{ss}	(4.14, 4.22)	(7.84, 7.84, 7.84)	481.72	0	83.4

Table A.2 $\text{Sr}^{2+}\text{Ti}_{0.75}^{4+}\text{Fe}_{0.25}^y\text{O}_{2.875}^{2-}$ properties for vacancies \mathbf{V}_{p_1} and \mathbf{V}_{p_2} (HSE06). FM and AFM energies of $nm_{\text{Fe}} \sim a'\sqrt{2}$ configurations for each initial $S_i^{1,2}$ Fe spins, as well as lattice parameters, magnetic structure, band-gap and relative energy of the selected gs and ss states.

y	$S_i^{1,2}$	\mathbf{V}_{p_1}		\mathbf{V}_{p_2}	
		E_{FM} (meV/f.u.)	E_{AFM} (meV/f.u.)	E_{FM} (meV/f.u.)	E_{AFM} (meV/f.u.)
(2+,4+)	h,h	112.4	0.001	94.0	0.001
	h,l	166.1	128.9	275.0	143.4
	l,h	230.9	165.6	210.7	193.2
	l,l	371.7	129.3	93.0	143.4
(4+,2+)	h,l	165.5	165.6	193.6	193.4
	l,h	217.4	129.2	319.8	142.0
	l,l	143.5	129.5	143.4	143.4
(3+,3+)	h,h	0.8 _{ss}	0.002	0.6 _{ss}	0.008
	h,l	166.1	165.6	273.7	194.0
	l,h	209.4	165.6	223.7	193.2
	l,l	371.8	— _{gs}	400.4	— _{gs}
State	$S_f^{1,2}(\mu_B)$	$(a', b', c') (\text{Å})$	$V (\text{Å}^3)$	E_{bg} (eV)	$\Delta E_{p_i^{gs}}$ (meV)
p_1^{gs}	(4.12, -4.19)	(7.83, 7.83, 7.86)	481.38	1.94	5.1
p_1^{ss}	(4.12, 4.19)	(7.83, 7.83, 7.85)	481.51	0	5.9
p_2^{gs}	(4.12, -4.20)	(7.84, 7.85, 7.83)	481.57	0	—
p_2^{ss}	(4.12, 4.20)	(7.84, 7.84, 7.83)	481.25	0	0.6

Table A.3 $\text{Sr}^{2+}\text{Ti}^{4+}\text{Fe}_{0.75}^y\text{O}_{2.875}^{2-}$ properties for vacancy V_{d_1} (HSE06). FM and AFM energies of $nm_{\text{Fe}} \sim a'\sqrt{3}$ configurations for each initial $S_i^{1,2}$ Fe spins, as well as lattice parameters, magnetic structure, band-gap and relative energy of the selected gs and ss states.

y	$S_i^{1,2}$	E_{FM} (meV/f.u.)	E_{AFM} (meV/f.u.)	
(2+,4+)	h,h	105.1	— ^{gs}	
	h,l	306.9	132.4	
	l,h	215.5	172.5	
	l,l	102.9	132.7	
(4+,2+)	h,l	273.3	172.3	
	l,h	231.0	132.9	
	l,l	144.0	132.4	
(3+,3+)	h,h	0.04 ^{ss_2}	0.1	
	h,l	174.2	172.3	
	l,h	215.2	172.3	
	l,l	382.9	0.1 ^{ss_1}	
State	$S_F^{1,2}$ (μ_B)	(a', b', c') (\AA)	V (\AA^3)	E_{bg} (eV)
d_1^{gs}	(4.12, -4.12)	(7.83, 7.83, 7.85)	481.83	2.04
$d_1^{ss_1}$	(4.12, -4.12)	(7.83, 7.83, 7.85)	481.51	0
$d_1^{ss_2}$	(4.12, 4.12)	(7.83, 7.83, 7.85)	481.62	0

A.3 Monte Carlo modeling

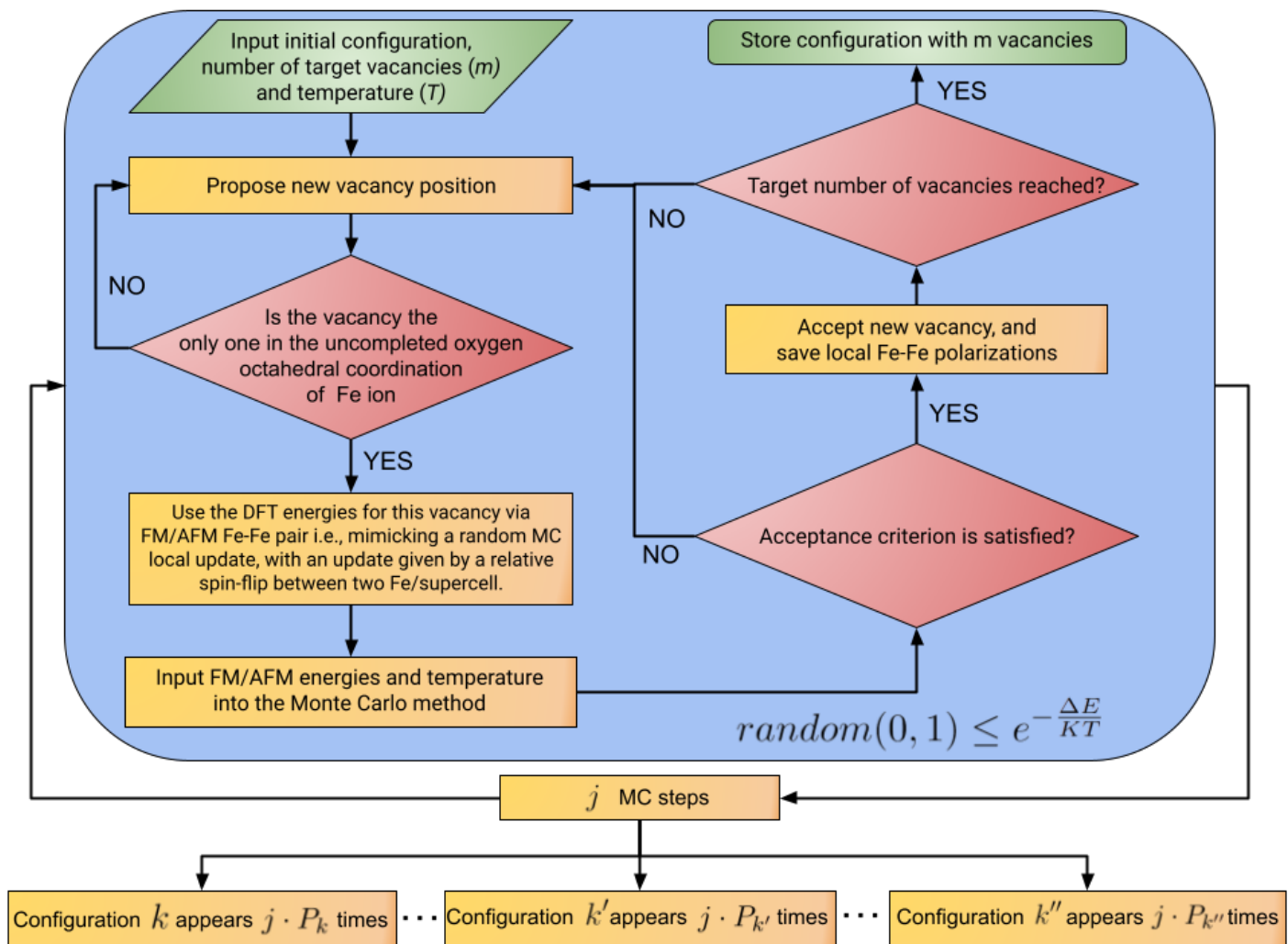


Fig. A.3 Diagram of the algorithm used to implement a Metropolis Monte Carlo scheme, which generates effective magnetic sites out of pairs of Fe ions constrained by uncompleted coordinating oxygen-octahedra. Such effective magnetic moments are averaged for every possible vacancy distribution to then calculate the spontaneous perovskite magnetization by using the probabilities of occurrence P_k of such distributions along with their configurational magnetization M_k , through Equation 1.

A.4 Oxygen and titanium sub-lattices

Table A.4 Magnetic moments of the O and Ti ions in the gs and ss configurations of Tables A.1, A.2 and A.3

100	$S_f(\mu_B)$		110	$S_f(\mu_B)$		111	$S_f(\mu_B)$
	V_{a_1}	V_{a_2}		V_{p_1}	V_{p_2}		V_{d_1}
	-	0.043		-0.093	-0.092		0.121
	0.000	0.043		-0.093	-0.095		0.121
	0.000	0.000		-0.093	-0.076		-0.094
	0.000	0.000		-0.093	-0.076		-0.094
	-0.002	0.002		0.002	0.002		0.000
	-0.002	0.002		0.002	0.002		0.000
	0.002	-0.002		0.002	0.008		0.000
	0.002	-0.002		0.002	0.003		0.000
	-0.002	0.006		-0.089	-0.097		0.006
	-0.002	0.002		-0.092	-0.097		0.006
	0.002	-0.001		0.000	0.000		0.000
	0.002	-0.002		0.000	0.000		0.000
	0.000	-0.001		0.006	0.000		0.000
	0.000	-0.001		0.006	0.000		0.000
	0.000	0.000		-	0.118		0.000
	0.000	0.000		0.095	0.118		0.000
	-0.101	-0.081		-0.002	-0.001		0.121
	-0.101	-0.081		-0.002	-0.002		0.121
	0.101	0.101		-0.002	-0.002		-0.094
	0.101	0.101		-0.002	-0.002		-0.094
	-0.101	-0.085		0.119	0.122		0.000
	-0.101	-0.084		0.119	0.122		0.000
	0.101	-		0.119	-		0.000
	0.101	0.083		0.119	0.101		0.000
ΣO	0.000	0.043	ΣO	0.030	0.056	ΣO	0.036
	-0.001	-0.001		-0.052	-0.051		-0.052
	0.001	0.001		0.047	0.047		0.047
	-0.047	-0.049		-0.052	-0.052		-0.052
	0.047	0.048		0.047	0.047		0.047
	-0.047	-0.049		-0.050	-0.050		-0.050
	0.047	0.050		0.052	0.049		0.052
ΣTi	0.000	0.000	ΣTi	-0.007	-0.013	ΣTi	-0.008

, respectively.

Notes and references

- 1 G. Rijnders and D. H. Blank, *Nature*, 2005, **433**, 369–370.
- 2 J. Wang, J. Neaton, H. Zheng, V. Nagarajan, S. Ogale, B. Liu, D. Viehland, V. Vaithyanathan, D. Schlom, U. Waghmare *et al.*, *science*, 2003, **299**, 1719–1722.
- 3 K. J. Choi, M. Biegalski, Y. Li, A. Sharan, J. Schubert, R. Uecker, P. Reiche, Y. Chen, X. Pan, V. Gopalan *et al.*, *Science*, 2004, **306**, 1005–1009.
- 4 H. Jang, A. Kumar, S. Denev, M. D. Biegalski, P. Maksymovych, C. Bark, C. T. Nelson, C. Folkman, S. H. Baek, N. Balke *et al.*, *Physical Review Letters*, 2010, **104**, 197601.
- 5 M. Fiebig, T. Lottermoser, D. Meier and M. Trassin, *Nature Reviews Materials*, 2016, **1**, 1–14.
- 6 E. A. Cortés Estay, S. P. Ong, C. A. Ross and J. M. Florez, *Magnetochemistry*, 2022, **8**, 144.
- 7 J. Khatua, T. Arh, S. B. Mishra, H. Luetkens, A. Zorko, B. Sana, M. S. R. Rao, B. R. K. Nanda and P. Khuntia, *Scientific Reports*, 2021, **11**, 1–14.
- 8 J. Xue, Z. Wang, A. Comstock, Z. Wang, H. H. Y. Sung, I. D. Williams, D. Sun, J. Liu and H. Lu, *Chemistry of Materials*, 2022, **34**, 2813–2823.
- 9 A. Stucky, G. W. Scheerer, Z. Ren, D. Jaccard, J.-M. Pouchiro, C. Barreteau, E. Giannini and D. Van Der Marel, *Scientific reports*, 2016, **6**, 1–9.
- 10 J. Schooley, W. Hosler and M. L. Cohen, *Physical Review Letters*, 1964, **12**, 474.
- 11 N. Reyren, S. Thiel, A. Caviglia, L. F. Kourkoutis, G. Hammerl, C. Richter, C. W. Schneider, T. Kopp, A.-S. Ruetschi, D. Jaccard *et al.*, *Science*, 2007, **317**, 1196–1199.
- 12 M. Kim, G. Duscher, N. D. Browning, K. Sohlberg, S. T. Pantelides and S. J. Pennycook, *Physical Review Letters*, 2001, **86**, 4056.
- 13 T. Goto, D. H. Kim, X. Sun, M. C. Onbasli, J. M. Florez, S. P. Ong, P. Vargas, K. Ackland, P. Stamenov, N. M. Aimon *et al.*, *Physical Review Applied*, 2017, **7**, 024006.
- 14 S. Song, H. Han, H. M. Jang, Y. T. Kim, N.-S. Lee, C. G. Park, J. R. Kim, T. W. Noh and J. F. Scott, *Advanced Materials*, 2016, **28**, 7430–7435.
- 15 M. Itoh, R. Wang, Y. Inaguma, T. Yamaguchi, Y. Shan and T. Nakamura, *Physical Review Letters*, 1999, **82**, 3540.
- 16 M. Choi, F. Oba, Y. Kumagai and I. Tanaka, *Advanced Materials*, 2013, **25**, 86–90.
- 17 C. Mitra, C. Lin, A. B. Posadas and A. A. Demkov, *Physical Review B*, 2014, **90**, 125130.
- 18 K. Klyukin and V. Alexandrov, *Physical Review B*, 2017, **95**, 035301.
- 19 A. Lopez-Bezanilla, P. Ganesh and P. B. Littlewood, *Appl Materials*, 2015, **3**, 100701.
- 20 A. Cammarata and J. M. Rondinelli, *Applied Physics Letters*, 2016, **108**, 213109.
- 21 O. O. Brovko and E. Tosatti, *Physical Review Materials*, 2017, **1**, 044405.
- 22 F. El-Mellouhi, E. N. Brothers, M. J. Lucero and G. E. Scuseria, *Physical Review B*, 2011, **84**, 115122.
- 23 Y.-Y. Pai, A. Tylan-Tyler, P. Irvin and J. Levy, *Reports on Progress in Physics*, 2018, **81**, 036503.
- 24 Y. Zhang, J. Wang, M. Sahoo, T. Shimada and T. Kitamura, *Physical Chemistry Chemical Physics*, 2015, **17**, 27136–27144.
- 25 C. Lin, C. Mitra and A. A. Demkov, *Physical Review B*, 2012, **86**, 161102.
- 26 J. R. Petrie, C. Mitra, H. Jeen, W. S. Choi, T. L. Meyer, F. A. Reboredo, J. W. Freeland, G. Eres and H. N. Lee, *Advanced Functional Materials*, 2016, **26**, 1564–1570.
- 27 X.-L. Dong, K.-H. Zhang and M.-X. Xu, *Frontiers of Physics*, 2018, **13**, 1–7.
- 28 D. Lee, H. Wang, B. A. Noesges, T. J. Asel, J. Pan, J.-W. Lee, Q. Yan, L. J. Brillson, X. Wu and C.-B. Eom, *Physical Review Materials*, 2018, **2**, 060403.
- 29 P. Sikam, P. Moontragoon, C. Sararat, A. Karaphun, E. Swatsitang, S. Pinitsoontorn and P. Thongbai, *Applied Surface Science*, 2018, **446**, 92–113.
- 30 Y.-G. Wang, X.-G. Tang, Q.-X. Liu, Y.-P. Jiang and L.-L. Jiang, *Nanomaterials*, 2017, **7**, 264.
- 31 Y. Zhang, O. Kurt, D. Ascenzo, Q. Yang, T. Le, S. Greenbaum, T. J. Bayer, C. A. Randall and Y. Ren, *The Journal of Physical Chemistry C*, 2018, **122**, 12864–12868.
- 32 G. F. Dionne, *Magnetic oxides*, Springer, 2009, vol. 14.
- 33 D. H. Kim, N. M. Aimon, L. Bi, J. Florez, G. F. Dionne and C. Ross, *Journal of Physics: Condensed Matter*, 2012, **25**, 026002.
- 34 J. Florez, S. Ong, M. Onbaşlı, G. Dionne, P. Vargas, G. Ceder and C. Ross, *Applied Physics Letters*, 2012, **100**, 252904.
- 35 A. Walsh, A. A. Sokol, J. Buckeridge, D. O. Scanlon and C. R. A. Catlow, *Electron counting in solids: Oxidation states, partial charges, and ionicity*, 2017.
- 36 M. A. Opazo, S. P. Ong, P. Vargas, C. Ross and J. M. Florez, *Physical Review Materials*, 2019, **3**, 014404.
- 37 Y.-Y. Pai, A. Tylan-Tyler, P. Irvin and J. Levy, *Reports on Progress in Physics*, 2018, **81**, 036503.

- 38 U. Aschauer and N. A. Spaldin, *Journal of Physics: Condensed Matter*, 2014, **26**, 122203.
- 39 Y. S. Kim, J. Kim, S. Moon, W. Choi, Y. Chang, J.-G. Yoon, J. Yu, J.-S. Chung and T. Noh, *Applied Physics Letters*, 2009, **94**, 202906.
- 40 M. Choi, F. Oba and I. Tanaka, *Physical review letters*, 2009, **103**, 185502.
- 41 K. Klyukin and V. Alexandrov, *Physical Review B*, 2017, **95**, 035301.
- 42 F. Yang, Q. Zhang, Z. Yang, J. Gu, Y. Liang, W. Li, W. Wang, K. Jin, L. Gu and J. Guo, *Applied Physics Letters*, 2015, **107**, 082904.
- 43 I. Hallsteinsen, M. Nord, T. Bolstad, P.-E. Vullum, J. E. Boschker, P. Longo, R. Takahashi, R. Holmestad, M. Lippmaa and T. Tybell, *Crystal Growth & Design*, 2016, **16**, 2357–2362.
- 44 I. Sokolović, M. Schmid, U. Diebold and M. Setvin, *Physical Review Materials*, 2019, **3**, 034407.
- 45 A. Abd El-Naser, E. Abdel-Khalek, E. Nabhan, D. Rayan, M. Gaafar and N. Abd El-Aal, *Philosophical Magazine*, 2021, **101**, 710–728.
- 46 X. Wang, Z. Wang, Q. Hu, C. Zhang, D. Wang and L. Li, *Solid State Communications*, 2019, **289**, 22–26.
- 47 A. S. Tang, M. C. Onbasli, X. Sun and C. A. Ross, *ACS applied materials & interfaces*, 2018, **10**, 7469–7475.
- 48 D. H. Kim, L. Bi, P. Jiang, G. F. Dionne and C. Ross, *Physical Review B*, 2011, **84**, 014416.
- 49 L. Bi, H.-S. Kim, G. F. Dionne and C. Ross, *New Journal of Physics*, 2010, **12**, 043044.
- 50 A. B. Posadas, C. Mitra, C. Lin, A. Dhamdhere, D. J. Smith, M. Tsoi and A. A. Demkov, *Physical Review B*, 2013, **87**, 144422.
- 51 A. Stukowski, *Modelling and simulation in materials science and engineering*, 2009, **18**, 015012.
- 52 G. Kresse and J. Furthmüller, *Physical review B*, 1996, **54**, 11169.
- 53 G. Makov and M. Payne, *Physical Review B*, 1995, **51**, 4014.
- 54 H. J. S. Ge and M. Ernzerhof, *J. Chem. Phys.*, 2006, **124**, 219906.
- 55 S. L. Dudarev, G. A. Botton, S. Y. Savrasov, C. Humphreys and A. P. Sutton, *Physical Review B*, 1998, **57**, 1505.
- 56 Y. Wang, F. Chen, L. Zheng, J. Gao and Y. Liu, *Chemical Physics Letters*, 2022, **805**, 139943.
- 57 S. P. Ong, W. D. Richards, A. Jain, G. Hautier, M. Kocher, S. Cholia, D. Gunter, V. L. Chevrier, K. A. Persson and G. Ceder, *Computational Materials Science*, 2013, **68**, 314–319.
- 58 A. Jain, S. P. Ong, G. Hautier, W. Chen, W. D. Richards, S. Dacek, S. Cholia, D. Gunter, D. Skinner, G. Ceder *et al.*, *APL materials*, 2013, **1**, 011002.
- 59 H. T. Stokes and D. M. Hatch, *Journal of Applied Crystallography*, 2005, **38**, 237–238.
- 60 P. D. Reyntjens, S. Tiwari, M. L. Van de Put, B. Sorée and W. G. Vandenberghe, *Materials*, 2021, **14**, 4167.
- 61 E. Zhurkin, M. Hou, J. Kuriplach, T. Ossowski and A. Kiejna, *Nuclear Instruments and Methods in Physics Research Section B: Beam Interactions with Materials and Atoms*, 2011, **269**, 1679–1683.
- 62 H. Shiiba, M. Nakayama, T. Kasuga, R. W. Grimes and J. A. Kilner, *Physical Chemistry Chemical Physics*, 2013, **15**, 10494–10499.
- 63 H. Ding, S. S. Dwaraknath, L. Garten, P. Ndione, D. Ginley and K. A. Persson, *ACS applied materials & interfaces*, 2016, **8**, 13086–13093.
- 64 M. K. Horton, J. H. Montoya, M. Liu and K. A. Persson, *npj Computational Materials*, 2019, **5**, 64.
- 65 M. Kuhn, J. J. Kim, S. R. Bishop and H. L. Tuller, *Chemistry of Materials*, 2013, **25**, 2970–2975.
- 66 J. Florez, J. Mazo-Zuluaga and J. Restrepo, *Hyperfine interactions*, 2005, **161**, 161–169.
- 67 J. Aramburu and M. Moreno, *The Journal of Physical Chemistry A*, 2021, **125**, 2284–2293.
- 68 H. A. Tahini, X. Tan, U. Schwingenschlögl and S. C. Smith, *ACS Catalysis*, 2016, **6**, 5565–5570.
- 69 J. P. Allen and G. W. Watson, *Physical Chemistry Chemical Physics*, 2014, **16**, 21016–21031.
- 70 D. Wang, S. Wei, A. Yuan, F. Tian, K. Cao, Q. Zhao, Y. Zhang, C. Zhou, X. Song, D. Xue *et al.*, *Advanced Science*, 2020, **7**, 2000566.
- 71 G. Katsikas, C. Sarafidis and J. Kioseoglou, *physica status solidi (b)*, 2021, **258**, 2000600.
- 72 Q. Tao, P. Xu, M. Li and W. Lu, *npj Computational Materials*, 2021, **7**, 23.
- 73 I. Østrøm, M. A. Hossain, P. A. Burr, J. N. Hart and B. Hoex, *Physical Chemistry Chemical Physics*, 2022, **24**, 14119–14139.
- 74 J. He and C. Franchini, *Physical Review B*, 2012, **86**, 235117.
- 75 P. Pokhilko and D. Zgid, *The Journal of Chemical Physics*, 2022, **157**, 144101.
- 76 K. Tada, S. Tanaka, T. Kawakami, Y. Kitagawa, M. Okumura and K. Yamaguchi, *Applied Physics Express*, 2019, **12**, 115506.
- 77 K. Tada, H. Koga, M. Okumura and S. Tanaka, *Chemical Physics Letters*, 2018, **701**, 103–108.